Impact of internal structure on aggregate collisions

Rahul Bandyopadhyay,[1] María Belén Planes,[2] Emmanuel N. Millán,[3] Eduardo M. Bringa[2,4] and Herbert M. Urbassek [1]★

[1]*Physics Department and Research Center OPTIMAS, University Kaiserslautern-Landau, Erwin-Schrödinger-Straße, D-67663 Kaiserslautern, Germany*
[2]*CONICET and Facultad de Ingenería, Universidad de Mendoza, Mendoza 5500, Argentina*
[3]*CONICET and ITIC, Universidad Nacional de Cuyo, Mendoza 5500 Argentina*
[4]*Centro de Nanotecnología Aplicada, Facultad de Ciencias, Universidad Mayor, Santiago 8580745, Chile*

ABSTRACT

Granular-mechanics simulations are used to study collisions between granular aggregates. We compare the collision outcomes for three different types of aggregate: (i) aggregates constructed by a ballistic particle–cluster aggregation (BPCA) process, and two homogeneous spherical aggregates which differ by their grain coordination. All aggregates contain the same number of grains and (central) filling factor. We find that BPCA aggregates have a slightly decreased growth velocity for central impacts. After scaling the collision velocities to the growth velocity for central impact and the impact parameter to the gyration radius, our collision results show a remarkable degree of agreement for the aggregates studied. Also, the collision-induced compaction as well as the size of fluctuations during the collision process are identical for all aggregate types. Even at glancing collisions, the larger extension and rough surface of BPCA aggregates do not cause major changes as compared to homogeneous aggregates with a well-defined and smooth surface. However, monomer ejection during the collision is enhanced for BPCA aggregates. This study thus shows that details of the internal aggregate structure are of little importance in collisions of granular aggregates, except for grain ejection.

Key words: methods: numerical – planets and satellites: formation – protoplanetary discs.

1 INTRODUCTION

Dust aggregates are ubiquitous in space; they are found in protoplanetary discs (Armitage 2011), in debris discs (Gáspár, Rieke & Balog 2013), in planetary rings (Burns, Hamilton & Showalter 2001), and in the interplanetary space (Grün 2007). Collisions between dust aggregates shape the evolution of these dust ensembles and dust clouds (Ormel et al. 2009; Birnstiel, Fang & Johansen 2016; Millán et al. 2023). Such collisions also form the first steps of dust agglomeration, which eventually leads to the formation of planetesimals and planets (Weidenschilling 1977; Weidenschilling & Cuzzi 1993; Armitage 2010; Blum 2018).

Collisions between dust aggregates have, therefore, been studied using both experimental (Wurm & Blum 1998; Blum 2010; Wurm & Teiser 2021) and simulational (Paszun & Dominik 2009; Wada et al. 2009; Ringl et al. 2012; Hasegawa et al. 2023) methods. In view of the applications mentioned above, often the question of whether the collisions lead to aggregate growth or erosion was in the centre of attention. For fixed properties of the grain material, this issue primarily depends on the aggregate masses and the relative velocity of the collision partners (Birnstiel et al. 2016; Blum 2018). Besides that, aggregate porosity (Gunkelmann, Ringl & Urbassek 2016; Planes et al. 2021; Bandyopadhyay, Umstätter & Urbassek 2023) and shape (Bandyopadhyay & Urbassek 2023) influence the collision outcomes.

In addition, it has been found (Wada et al. 2008, 2009) that aggregates with fractal dimension D considerably below 3 – such as those constructed using a ballistic cluster–cluster aggregation algorithm, $D = 2$ – have a strongly changed collision dynamics as compared to space-filling aggregates with $D = 3$. Low-dimensional fractal aggregates are more easily destructed in collisions because grains dissociated by the aggregates during the collision find sufficient space to escape and are no longer integrated in the surviving aggregate or a fragment.

The question as to what extent the internal aggregate structure influences the collision dynamics has hitherto been only little investigated. Wada et al. (2011) studied the influence of grain coordination in collisions and found that high coordination favours aggregate bouncing. However, in this study higher-coordinated aggregates also have a higher filling factor such that the influence of coordination alone could not be clarified.

Aggregates with different grain coordination distributions may originate from different production processes. Ballistic particle–cluster aggregation (BPCA) mimics a growth process where a dust nucleus grows by the addition of monomer grains; such aggregates have therefore been widely investigated in previous simulations (Paszun & Dominik 2009; Wada et al. 2009; Hasegawa et al. 2021). However, BPCA aggregates have an intrinsically non-uniform structure; besides a rough surface, their density decreases from the centre to the periphery. On the other hand, aggregates may form from (collision-induced) fragmentation processes of larger bodies – besides dust particles, also comets or asteroids (Jutzi et al. 2015) – and possess, therefore, a more homogeneous structure. For this

★ E-mail: urbassek@rhrk.uni-kl.de

reason, homogeneous aggregates also have been investigated in the past (Ringl et al. 2012; Gunkelmann et al. 2016; Bandyopadhyay et al. 2023).

In this study, we explore to what extent the internal structure of an aggregate influences aggregate collisions. We focus on space-filling aggregates with a fractal dimension close to 3. By keeping the total aggregate mass and the filling factor – at least close to the aggregate centre – at identical values, the study identifies the influence of grain coordination on the collision dynamics and outcomes. Even though in the aggregates considered here the average coordination is 2 – due to the construction process – the distributions of the coordination number vary strongly. This study also allows us to understand the deviations of collision outcomes between spherical homogenous and BPCA aggregates.

2 METHODS

2.1 Granular mechanics

Granular aggregates are composed of a number N of identical spherical grains of radius r_g. For specificity, we consider a model of silica grains where $r_g = 0.76 \, \mu$m. The material constants relevant for describing the interaction of the grains are given by the mass density $\rho = 2000 \, \text{kg m}^{-3}$, the specific surface energy $\gamma = 0.025 \, \text{J m}^{-3}$, Young's modulus $Y = 54 \, \text{GPa}$, and the Poisson ratio $\nu = 0.17$ (Chokshi, Tielens & Hollenbach 1993; Blum & Schräpler 2004; Ringl & Urbassek 2012).

The forces and torques acting when grains are in contact are described by a model of Chokshi et al. (1993) and Dominik & Tielens (1995, 1996, 1997) who define the normal and tangential forces as well as rolling and twisting torques that originate in grain–grain contacts. Details on these quantities are presented by Ringl & Urbassek (2012).

Let us denote the position of grain i in an aggregate by $\boldsymbol{x}_i$, where the origin of the coordinate system has been put in the centre of mass of the aggregate. Forces and torques between two grains i and j only act if the grain touch, i.e. if the grains overlap, $\delta = 2R - |\boldsymbol{x}_i - \boldsymbol{x}_j|$ is positive. The equilibrium overlap δ_{equ} between two grains is determined by the cancellation of the attractive and repulsive forces between the two grains. Following Dominik & Tielens (1997), the repulsive normal force is modelled by a Hertzian law, $F_r = [2Y/3(1 - \nu^2)](r_g/2)^{1/2}\delta^{3/2}$, while attraction is given by $F_a = -2\pi\gamma r_g$. The two forces cancel at an equilibrium overlap of $\delta_{\text{equ}} = 3.01 \, \text{Å}$. We note that in a dynamic situation, a dissipative (velocity-proportional) force also acts in normal direction, which does, however, not affect the static equilibrium overlap.

For the collision simulations, the motion of the grains, as well as the dynamics of the forces and torques are followed using the software LIGGGHTS (Kloss et al. 2012; Gunkelmann et al. 2016). In order to resolve grain–grain collisions, a time-step of 50 ps is adequate (Ringl & Urbassek 2012).

2.2 Aggregate construction

All aggregates considered consist of a number of $N = 20\,000$ grains and have identical filling factor $\Phi = 0.24$. The filling factor is defined as the ratio of the volume filled by grain material, $V_g = N(4\pi/3)r_g^3$, and the aggregate volume, V. For a spherical aggregate of radius R, it is hence

$$\Phi = N \left(\frac{r_g}{R} \right)^3. \tag{1}$$

Table 1. Overview of aggregates used. R_{gyr}: gyration radius. R_{equ}: equivalent radius. $\langle Z \rangle$: average coordination number. ΔZ: standard deviation of coordination number.

	RPCA	LPCA	BPCA1	BPCA2	BPCA3
R_{gyr} (r_g)	33.03	33.43	36.09	35.92	35.79
R_{equ} (r_g)	42.64	43.16	46.60	46.37	46.20
$\langle Z \rangle$	2.001	2.002	2.000	2.000	2.000
ΔZ	0.384	1.474	0.945	0.948	0.948

We use three types of aggregates: two homogeneous spherical aggregates denoted by local particle-cluster attachment (LPCA) and random particle–cluster attachment (RPCA), which differ in their internal structure, and an aggregate constructed using a BPCA algorithm. These will be described in the following.

Spherical aggregates are constructed by placing the N grains successively in a spherical volume with the radius of the aggregate defined by equation (1). For the values chosen for N and Φ, this gives a radius of $R = 43.68r_g$.

The simplest algorithm is the one used for building RPCA aggregates: We place the first grain at the origin of the sphere. Then we iterate the following algorithm until N grains are placed: we attach a new grain to a randomly chosen grain in random direction. This attachment occurs at a distance of $2r_g - \delta_{\text{equ}}$, where δ_{equ} is the equilibrium overlap of two grains. If the newly added grain i is not entirely within the prescribed aggregate shape, i.e. $|\boldsymbol{x}_i| \leq R - r$, or if its distance to another grain is smaller than $2r_g - \delta_{\text{equ}}$, it is deleted, otherwise it is kept. This procedure is repeated until the total number of grains reaches N.

The algorithm for constructing LPCA aggregates uses a modification based on the notion of a local filling factor Φ_i around grain i (Ringl & Urbassek 2012, 2013; Ringl et al. 2012). It is defined via the volume filled by grain material in a sphere of radius r_c around grain i in analogy to equation (1). In this study, we use $r_c = 5r_g$. The construction of this type of aggregates modifies the above procedure in the selection of the grain to which the next grain is attached: rather than selecting a random grain, it chooses the grain with the smallest local filling factor. In addition, if grain i is attached outside the outer aggregate boundary, $|\boldsymbol{x}_i| > R$, it is not discarded but marked as a 'ghost grain' (Planes et al. 2021); such ghost grains are taken into account when calculating the local filling factor but are not included in the aggregate.

BPCA aggregates are grown by simulating a random deposition process in which monomers are added to the growing aggregate from random directions; the grains fall on linear trajectories until they hit the aggregate and stick at this point ('ballistic aggregation'; Mukai et al. 1992). We produce the aggregates by an open software (Bentley 2019) which is based on a ray-tracing algorithm. In contrast to the homogeneous aggregates described above, these aggregates have a rough surface; due to shadowing effects, the internal structure is more prone to containing voids than the homogeneous aggregates. We constructed aggregates BPCA1, 2, and 3 with properties listed in Table 1; they differ only by the chosen random directions for deposition.

After construction, all aggregates are relaxed by running a short simulation (25 000 time-steps) to reduce any tangential and normal forces that might have built up during the construction process and to guarantee that all grain–grain contacts reach equilibrium overlap.

2.3 Aggregate collisions

The same code and the same material parameters were used for all collisions. To start the collision, two identical aggregates were placed

such that their centres are located at a distance d. We used $d = 88.68r_g$ for homogeneous aggregates and $d = 118.42r_g$ for BPCA aggregates, such that the two aggregates do not interact initially. In order to increase statistics, both aggregates were rotated by a random angle before starting the collision. For BPCA aggregates, five rotations were considered, and also for central collisions of the homogeneous aggregates; for oblique collisions of central aggregates, only one rotation was used. To start the collision, the aggregates were given a relative velocity v, which was varied between 2.5 and $20\,\mathrm{m\,s^{-1}}$ in steps of $2.5\,\mathrm{m\,s^{-1}}$. All collisions were monitored in the centre-of-mass system. Simulations are followed for up to $200\,\mu$s after the start of the collision.

3 RESULTS AND DISCUSSION

3.1 Aggregate properties

Fig. 1 presents the aggregates considered in this study highlighting their internal structure using the coordination number Z. As Table 1 demonstrates, the average coordination number equals $\langle Z \rangle = 2$ for all aggregates; however, the standard deviations are considerably different. The shapes of the distribution, Fig. 1, are also widely different: The RPCA aggregates are mainly two-fold coordinated, that is they form long chains; the numbers of chain branching points ($Z = 3$) as well as of chain ends ($Z = 1$) are below 10 per cent. As the snapshots show, both chain ends and branching points are found as well on the aggregate surface and in its interior.

The LPCA aggregates show a strongly changed coordination, in which singly connected grains prevail; therefore, chains are short. As a compensation, many branching points exist, in which grains are coordinated with up to eight other grains. Again, the snapshots demonstrate that not only chain ends but also highly coordinated grains are present both on the aggregate surface and in its interior.

BPCA aggregates have a coordination distribution which is somewhat in between that of RPCA and LPCA aggregates. The most probably coordination is $Z = 2$ and a dominance of chain-like structures is indeed evident in the snapshots, in particular inside the aggregate. The chains are longer than for the LPCA aggregates and branching points are less frequent and have a maximum of five neighbouring grains.

In Fig. 1, we also display the radial distribution of the filling factor, $\Phi(r)$. It is calculated by determining the number of grains contained in spherical shells of width $2r_g$ around the aggregate centre. Both the LPCA and RPCA aggregates show a flat $\Phi(r)$ profile, in line with a homogeneous internal structure. Close to the centre, $\Phi(r)$ shows larger fluctuations caused by the small number of grains present in the innermost shells. Towards the outer boundary of the RPCA aggregates, the filling factor drops, since grain attachment outside the boundary is prohibited. For the LPCA aggregate, a slight increase in filling factor close to the boundary is discernible which is caused by the use of ghost grains in the construction process, see Section 2.2.

In contrast, BPCA aggregates have no fixed outer boundary and are hence characterized by a smooth drop-off of the $\Phi(r)$ profile extending to about $60r_g$, around 35 per cent beyond the radius $R = 43.68r_g$ of the homogeneous spheres. This is caused by the spatially unrestricted grain addition process during aggregate construction, see Section 2.2. We note that in the central part of the aggregate – inside $0.5R_{\mathrm{gyr}}$ – the BPCA filling factor amounts to 0.26. When averaging the filling factor over the convex hull of the entire aggregate, it is only in the range of 0.14–0.15, slightly depending on the aggregate; such a value is in agreement with previous studies (Kozasa, Blum & Mukai 1992; Blum & Schräpler 2004; Paszun & Dominik 2009).

In order to put the aggregate analysis on the same footing, we use the gyration radius R_{gyr}, which is determined from the positions of the centres, $\boldsymbol{x}_i$, of grains i (calculated with respect to the centre of mass of the aggregate) as

$$R_{\mathrm{gyr}}^2 = \frac{1}{N} \sum_i \boldsymbol{x}_i^2. \tag{2}$$

As for a homogeneous sphere of radius R, it is $R_{\mathrm{gyr}} = \sqrt{3/5}R$, we define an equivalent radius, R_{equ}, as

$$R_{\mathrm{equ}} = \sqrt{5/3}R_{\mathrm{gyr}}. \tag{3}$$

Table 1 shows that the equivalent radius of the homogeneous spheres is indeed close to the nominal radius $R = 43.68r_g$. R_{equ} underestimates R due to the construction process, in which grains are only inserted if they are fully inside R, that is if $|\boldsymbol{x}| \leq R - r_g$. The small deviations between the LPCA and RPCA aggregates are caused by the details of the respective construction algorithms.

Note that the equivalent radii of BPCA aggregates are systematically larger than those of homogeneous spheres, due to the more extended $\Phi(r)$ profile; the difference is, however, small and amounts to less than 10 per cent. Since for our collision study three different BPCA aggregates were constructed, we present their characteristics individually in Table 1. Differences in coordination are below 3 per mille and differences in the equivalent radius below 9 per mille.

Finally, we calculated the fractal dimension of the aggregates from the radial dependence of the number of grains within the aggregate (Meakin 1985). All aggregates have values close to 3, as expected from the space-filling construction process. For BCPA clusters, it is indeed expected on theoretical grounds – and demonstrated by simulations – that for large grain numbers N, the fractal dimension will approach 3 (Meakin 1999).

According to recent models and simulations, aggregate strength is a function of fractal dimension and filling factor (Tatsuuma, Kataoka & Tanaka 2019). Recent studies show that aggregate strength depends on the rolling energy parameter (Tatsuuma et al. 2023). Therefore, it is expected that all aggregates used in this study would have similar strength, despite their different topologies.

3.2 Central collisions

We first focus on central collisions. Fig. 2 a analyses the growth ratio, which is defined as the size of the largest post-collision aggregate, N_1, relative to the initial aggregate size, N,

$$n_{\mathrm{gr}} = N_1/N. \tag{4}$$

Evidently, $n_{\mathrm{gr}} > 1$, means growth of one of the collision partners, while $n_{\mathrm{gr}} < 1$ means that both colliding aggregates lost mass during the collision. Data shown are averages over five simulations for the homogeneous aggregates and over 15 simulations for the BPCA aggregates.

At small velocities, the two colliding aggregates merge to a single aggregate, which is denoted as the fused aggregate. With increasing velocity, the size of the fused aggregate decreases due to grain losses and – for larger velocity – the onset of fragmentation processes. A value of $n_{\mathrm{gr}} = 1.5$ (Bandyopadhyay et al. 2023) can be used to separate the low-velocity fusion regime, which is governed by a plateau in n_{gr}, from a steeper decline of the growth ratio. The velocity where $n_{\mathrm{gr}} = 1$ is denoted as the growth velocity for central impacts and will be denoted by v_{gr}^0.

Fig. 2a shows only small differences between the velocity dependence of n_{gr} for the aggregates used. In particular, the two
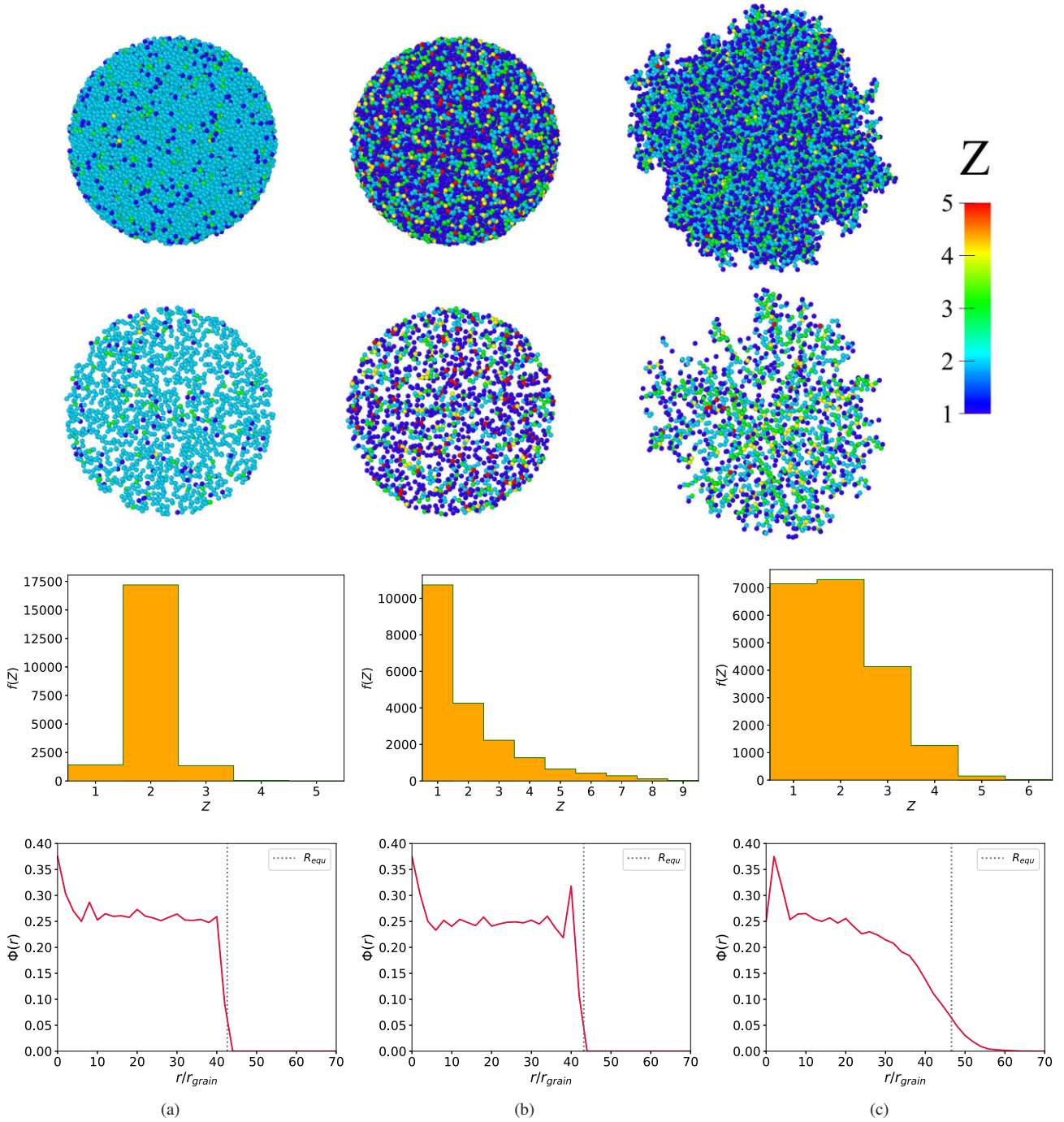
Figure 1. Structural properties of the aggregates used in this study: (a) RPCA, (b) LPCA, and (c) BPCA 1. Top row: Perspective view. Grain colouring by coordination number Z; red colour denotes $Z \geq 5$. Second row: central cross section, slice of thickness $4r_g$. Grain colouring by coordination number Z. Third row: distribution of coordination number Z. Fourth row: radial distribution of filling factor Φ. The equivalent radius, see Table 1, is marked by a vertical line.

homogeneous aggregates, LPCA and RPCA, show almost identical results. However, the growth ratio for the BPCA aggregates are somewhat below that of the homogeneous aggregates for all velocities. This appears to be a systematic effect, outside of the error bars of the simulations. It is caused by the higher probability with which boundary grains – or groups of grains – may be emitted in the collision from the rough aggregate surface of BPCA aggregates. The reduction in n_{gr} also leads to a decrease of the growth velocity of BPCA aggregates. We determined $v_{gr}^0 = 12.8\ (15.1, 14.1)\,\mathrm{m\,s^{-1}}$

or the BPCA (RPCA, LPCA) aggregates. The difference between the results for the RPCA and LPCA aggregates seems to be caused by the large statistical error in this case, such that we accept a value of $14.6\,\mathrm{m\,s^{-1}}$ as the average over the homogeneous aggregates. The value for the BPCA aggregates is reduced by 12 per cent relative to the average value of homogeneous aggregates; this result appears to be outside the error bars and hence statistically reliable.

Fig. 2b shows the standard deviation of the distribution of the largest-fragment size, N_1, as obtained from our simulations. Note

(a)   (b)
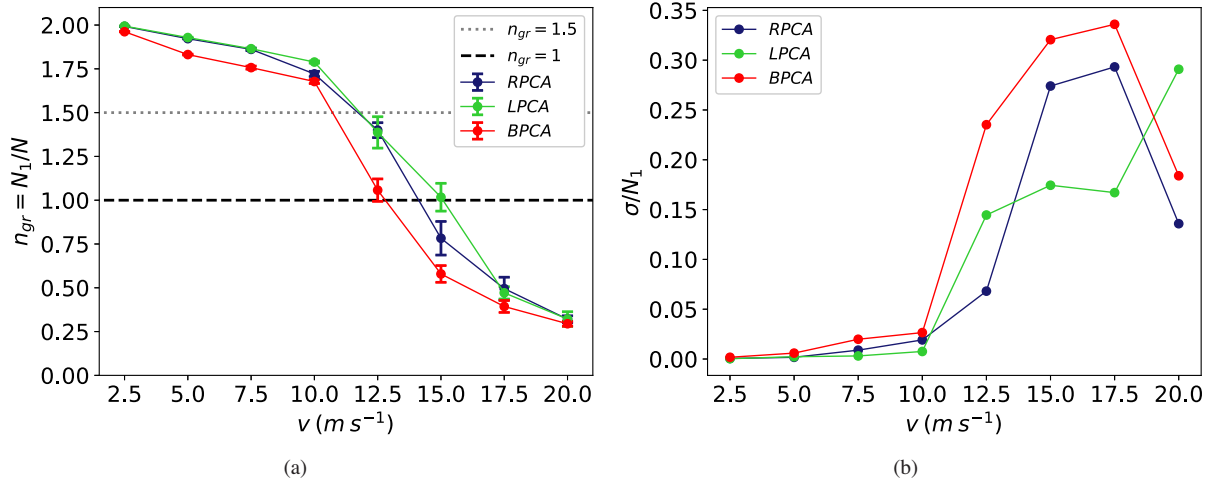
Figure 2. Dependence of the growth ratio, n_{gr}, on collision velocity v for central collisions. Error bars show the mean error of the average. The values of $n_{gr} = 1$ and 1.5 are marked by dashed horizontal lines. (b) Standard deviation of the size of the largest fragment, N_1.

(a)   (b)
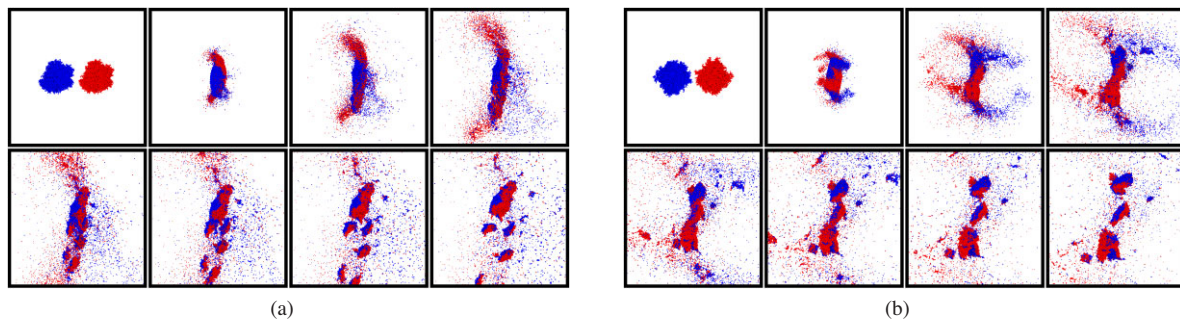
Figure 3. Series of snapshots (time difference $10\,\mu s$) showing the time evolution of BPCA aggregates at velocity $v = 15\,\mathrm{m\,s^{-1}}$ for central impacts. (a) shows the event with largest ($N_1 = 20331$) and (b) with the smallest ($N_1 = 6383$) fragment, while the average over all simulated cases is $\langle N_1 \rangle = 11580$. Grains are coloured according to their initial aggregate affiliation.

that this is not the error of the average value plotted in Fig. 2a, but an indicator of the width of the distribution. It shows that variations are particularly large near the growth velocity. At smaller velocities, collisions systematically lead to aggregate fusion with little variations; at larger velocities, erosion processes are strong and reduce the size of the largest fragment systematically, thereby also shrinking fluctuations. Around the growth velocity, however, fluctuations are large, since in some events the influence of aggregate fusion is larger, and in others the fragmentation processes. The small differences of local grain position and coordination are responsible for such differences.

Fig. 3 illustrates the fluctuations for events near the growth velocity for the case of BPCA aggregates by displaying snapshots for the event with the largest and the smallest N_1. While the evolution during the first (roughly) $40\,\mu s$ of the collision is very similar, the break-up of the merged aggregate into smaller fragments is distinctly different during the later stages of the collision. In Fig. 3a, a larger fragment is accompanied by several small aggregates, while in Fig. 3b, a smaller number of roughly equal-sized fragments are generated.

One might have expected that fluctuations in the BPCA aggregates were substantially larger than in the homogeneous aggregates. However, all aggregates show comparable standard deviations. Note that the relative error of the standard deviation σ is given by $\sigma/\sqrt{2(n-1)}$ where n is the number of simulations used (Berendsen 2011); thus

the differences between the standard deviations shown in Fig. 2b are statistically not relevant.

3.3 Compaction

Collisions modify the granular material of the aggregates; in particular, the collision zone is compacted. Compaction may be discussed using the local coordination numbers Z. We show the events leading to compaction in Fig. 4 for the three aggregates considered in a series of snapshots. Central collisions with a velocity of $7.5\,\mathrm{m\,s^{-1}}$ have been selected. The snapshots for the BPCA aggregates have been selected at larger times, since due to their rougher surface, the start of aggregate compaction occurs later than for the homogeneous aggregates.

Fig. 4 colours the grains based on their local coordination in order to indicate changes caused by the collision (Planes et al. 2020). We discuss the time evolution of the collision for the example of the LPCA aggregates. At the earliest time when the two aggregates have just started colliding, at $0.5\,\mu s$, grains are dissociated from the aggregate; the 0-coordinated grains show up in blue in Fig. 4. This dissociation front moves towards the aggregate interior and forms a lens-like structure at $2.5\,\mu s$. Inside this structure, grains have again found contact to other grains such that the coordination has increased,
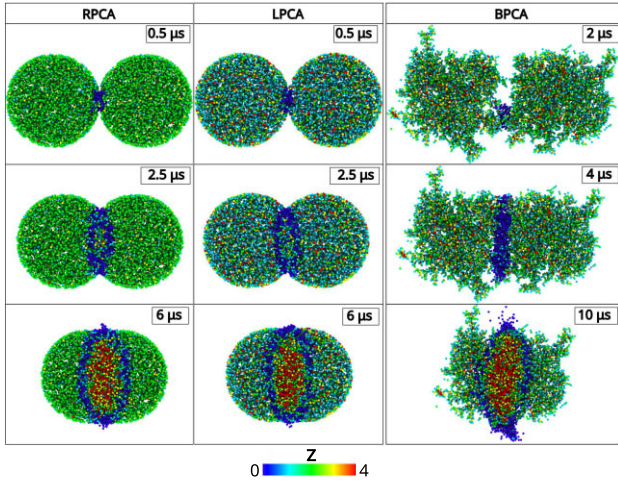
Figure 4. Time evolution of a central collision at $v = 7.5\,\mathrm{m\,s^{-1}}$ for the (a) LPCA, (b) RPCA, and (c) BPCA1 aggregates. Grains are coloured according to their coordination number. Red colours denote a coordination of $Z \geq 4$, while blue denotes dissociated grains, $Z = 0$.
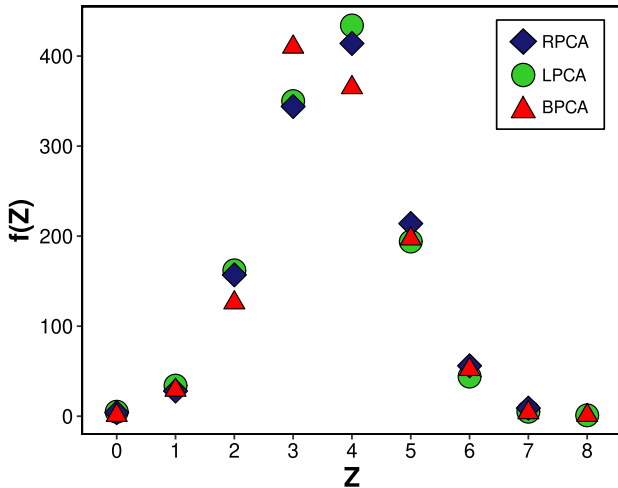

Figure 5. Distribution of the coordination number Z in the collision zone in the final panel of Fig. 4.

$Z \geq 1$. At later times, $6\,\mu\mathrm{s}$, when the dissociation front has further expanded, the collision zone has acquired a high coordination, $Z \geq 4$.

Interestingly, the sequence of events is very similar for the other aggregates studied, even for the BPCA aggregate. In the latter, due to its rougher surface, the collision does not start along the axis joining the centres of the two aggregates, but slightly shifted, at $2\,\mu\mathrm{s}$. However, already at $4\,\mu\mathrm{s}$, the dissociation front has assumed a symmetric shape, and at $10\,\mu\mathrm{s}$, the lens-shaped front shows great similarities with that in the homogeneous aggregates. In particular, the material within the collision zone inside the dissociation front has reached high values of coordination.

In Fig. 5, we compare the distribution of coordination numbers Z in the centre of the collision zone for the last frame of the three aggregate collisions illustrated in Fig. 4. Data have been obtained in a sphere around the centre of mass of the two colliding aggregates; its radius is $13.2r_{\mathrm{g}}$ such that the sphere is entirely contained within the compacted region inside the dissociation front. Note that the collision zone includes a slightly different number of atoms for each aggregate.
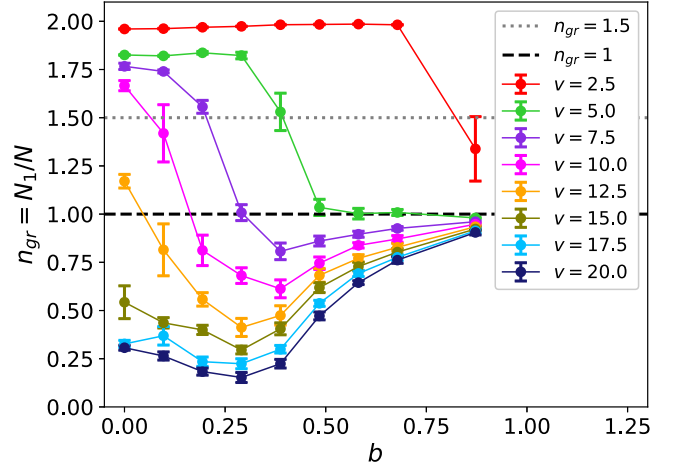
Figure 6. Dependence of the growth ratio, n_{gr}, on the scaled impact parameter b for various velocities v (in units of $\mathrm{m\,s^{-1}}$). Data are for the BPCA1 aggregate.

The filling factor in this sphere has increased to a value of 0.54 (0.54, 0.52) for RPCA (LPCA, BPCA) aggregates demonstrating the collision-induced compaction occurring. Fig. 5 shows that the coordination in the compacted zone has considerably increased and shows now a broad distribution around the average value of 4. The mean value of Z amounts to 3.67 (3.60, 3.63) for RPCA (LPCA, BPCA) aggregates with a standard deviation of 1.17 (1.15, 1.12).

These data as well as the Fig. 5 show that the coordination distribution for the three aggregates considered closely coincide. This is reasonable since the collision itself first dissociated all grains in this volume, thus dissolving the original structure. When subsequently the grains find new neighbours and organize themselves in a compacted structure, they thus start from the same disordered and uncoordinated state such that it is plausible that they organize themselves in similar structures.

3.4 Oblique collisions

Data for oblique collisions have been obtained as average over five simulations for the BPCA aggregates; here, rotated initial configurations of the BPCA1 aggregate have been used. For the homogeneous aggregates, only a single simulation has been performed for each velocity and impact parameter studied.

We scale the impact parameter B with the equivalent aggregate diameter, $2R_{\mathrm{equ}}$,

$$b = B/(2R_{\mathrm{equ}}). \tag{5}$$

The influence of the impact parameter on the growth ratio is shown in an exemplary way in Fig. 6 for the BPCA aggregates. We can discuss it as follows:

(i) For central collisions, $b = 0$, the growth ratio decreases monotonically with velocity, as discussed in detail in Section 3.2.

(ii) For large impact parameters, $b \geq 1$, the two aggregates would pass each other without interaction such that $n_{\mathrm{gr}} = 1$.

(iii) For the smallest velocity, $2.5\,\mathrm{m\,s^{-1}}$, aggregates fuse to form a merged aggregate containing almost $2N$ grains for all impact parameters. Only for almost glancing collisions, $b = 0.875$, n_{gr} drops. Fig. 7 illustrates the reason why even at such low velocities, the merged aggregate may break up into two fragments.

(iv) For larger velocities, $v \geq 7.5\,\mathrm{m\,s^{-1}}$, the dependence of the growth ratio on b is non-monotonic. n_{gr} shows a minimum at a finite
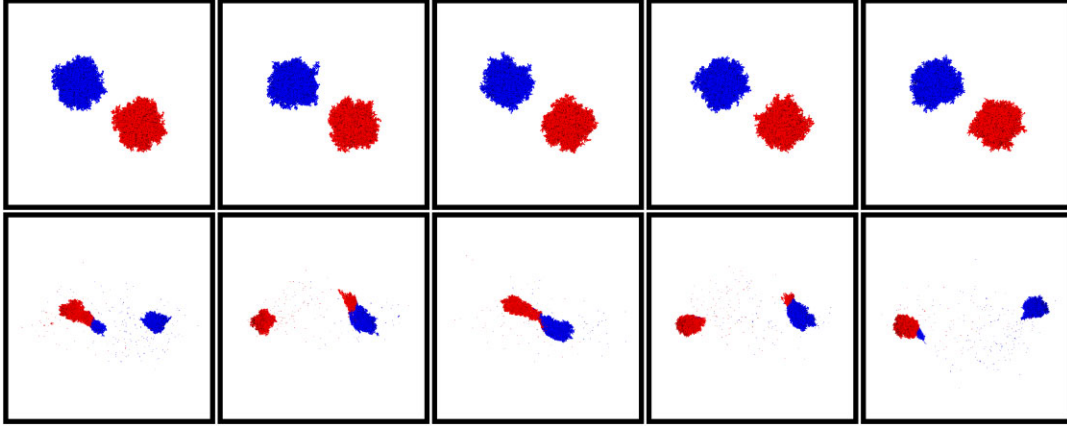
Figure 7. Snapshots showing the initial (top) and final (bottom) states (time $200\,\mu$s) of BPCA aggregates colliding at velocity $v = 2.5\,\mathrm{m\,s^{-1}}$ with an impact parameter of $b = 0.875$. Snapshots differ by the initial orientation of the two colliding aggregates. Grains are coloured according to their initial aggregate affiliation. The width of the boxes in the lower row is twice as that of the boxes on the upper row. Only in the third event, the merged aggregate survives, while it is torn apart by the centrifugal forces in all other events.

impact parameter, which we denote by b_{min}. At all velocities $v \geq 7.5\,\mathrm{m\,s^{-1}}$, $n_{\mathrm{gr}} < 1$ at b_{min}; this means that the collision leads to aggregate destruction.

(v) With increasing velocity, b_{min} decreases ($b_{\mathrm{min}} = 0.39$ for $v = 7.5$ and $10\,\mathrm{m\,s^{-1}}$ and 0.29 for higher velocities). This appears plausible from the fact that $v \cdot b_{\mathrm{min}}$ can be understood as the angular momentum necessary for the destruction of the temporarily forming merged aggregate. With increasing velocity, even aggregates formed at smaller impact parameters are disrupted.

We plot these data again in Fig. 8 in the form of a contour plot. Here, the results for all three aggregate classes studied are presented. In order to allow for easy comparison, we scale the velocity to the growth velocity for central impact,

$$\tilde{v} = v / v_{\mathrm{gr}}^0. \tag{6}$$

In addition, we classify each collision outcome into three classes (Bandyopadhyay et al. 2023) – fusion, sliding, or fragmentation – as follows: (i) Fusion, if $n_{\mathrm{gr}} \geq 1.5$. (ii) Sliding (or bouncing), if the size of the second-largest post-collision aggregate N_2 fulfils $N_2/N \geq 0.75$; then the largest post-collision aggregate has $N_1/N \leq 1.25$ and hence two more or less equal-sized large fragments remain. Note that for large impact parameters, $b = 1$, sliding is expected, since the clusters will pass each other apart from surface roughness. (iii) Fragmentation in all other cases.

Fig. 8 displays a surprising similarity between the aggregate collisions of the various aggregates studied throughout the (b, v) space explored. For central collisions, this similarity has been guaranteed by the velocity scaling. The simulation results show that this is also the case for oblique collisions. In particular, the lines characterizing the fusion regime, $n_{\mathrm{gr}} = 1.5$, and the 'growth line' $n_{\mathrm{gr}} = 1$ are similar in all cases.

The largest deviations occur in the region of ($b \sim 0.5$, $\tilde{v} \sim 0.5$); this is the region where the three collision outcomes (fusion, sliding, and fragmentation) meet. For brevity, we denote it as the 'centre' of the b–v plane. However, in this region also fluctuations are large. This is shown in Fig. 9 for BPCA aggregates: fluctuations of the size of the largest aggregate are largest along the growth line $n_{\mathrm{gr}} = 1$ and hence where the fragmentation regime sets in, and in particular also at the 'centre' of the b–v plane.

The fluctuations near the 'centre' of the b–v plane are illustrated for the case of BPCA aggregates in Fig. 10. At the impact parameter chosen, $b = 0.3875$, the two colliding aggregates form a temporarily merged aggregate that rotates around its centre of mass. In both events shown, it is eventually disrupted; however, in Fig. 10a the central part of the merged aggregate remains intact and only the outer parts are shed off, leading to a large post-collision fragment ('fusion' class), while in Fig. 10b, the merged aggregate breaks apart along the collision plane separating the original aggregates and leads to two large fragments ('sliding' class).

3.5 Impact-parameter average

Since in experiment, impact parameters typically cannot be controlled, averages over impact parameters must be used. The impact-parameter-averaged growth ratio, $\langle n_{\mathrm{gr}} \rangle$, as a function of collision velocity v is determined as

$$\langle n_{\mathrm{gr}}(v) \rangle = \frac{2\pi \int_0^{B_{\mathrm{max}}} n_{\mathrm{gr}}(B; v) B\, \mathrm{d}B}{\pi B_{\mathrm{max}}^2}. \tag{7}$$

Here we use $B_{\mathrm{max}} = 2R_{\mathrm{equ}}$, since collisions with larger impact parameters lead – even for BPCA aggregates – always to $n_{\mathrm{gr}} = 1$, see Section 3.4.

Fig. 11 shows the velocity dependence of this quantity for the aggregates studied. The average growth velocity, $\langle v_{\mathrm{gr}} \rangle$, is defined as the velocity where $\langle n_{\mathrm{gr}} \rangle = 1$; it is astonishingly insensitive to the aggregate type used. Its value is $\langle v_{\mathrm{gr}} \rangle = 7.5\,\mathrm{m\,s^{-1}}$ and is hence a factor of around 40–50 per cent below the central growth velocity, v_{gr}^0. The reduction of the impact-parameter-averaged growth velocity with respect to the growth velocity for central impacts is caused by the slope of the growth line $n_{\mathrm{gr}} = 1$ in the b–v plane, which moves to smaller velocities with increasing impact parameter b, see Fig. 8.

It is tempting to interpret the 'plateau' visible in Fig. 11 for the homogeneous spherical aggregates at $v = 5$–$7.5\,\mathrm{m\,s^{-1}}$ as a hint of a bouncing regime. Such a bouncing regime is found in experiments between low-velocity sticking and high-velocity fragmentation outcomes (Langkowski, Teiser & Blum 2008; Beitz et al. 2011; Weidling, Güttler & Blum 2012). However, the statistical basis for such an interpretation in our simulations appears to be too poor to allow such a conclusion. Also, recent simulation work (Arakawa et al. 2023) points out that bouncing becomes an important
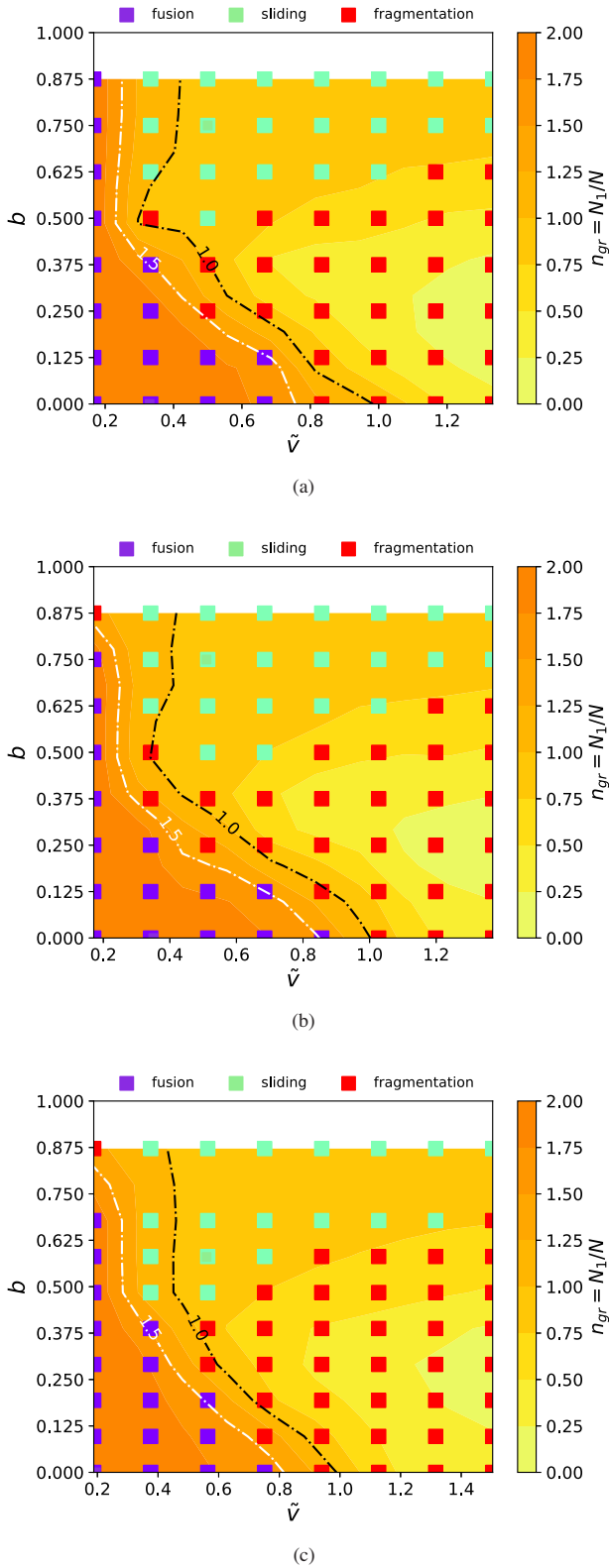
(a)

(b)

(c)

Figure 8. Dependence of the growth ratio on scaled collision velocity $\tilde{v}$ and scaled impact parameter b. (a) RPCA (b) LPCA (c) BPCA1.
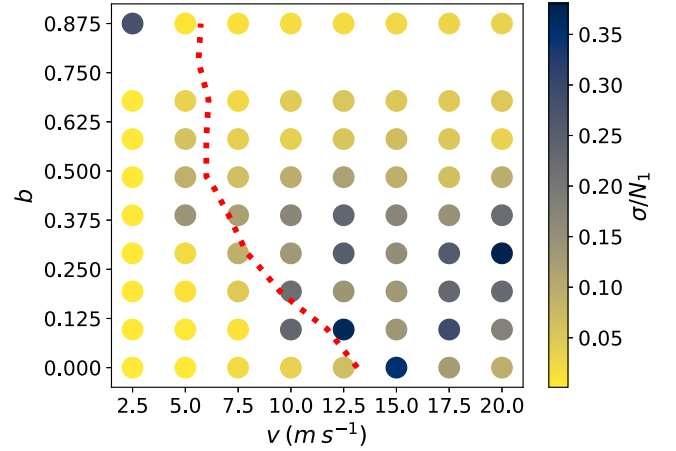

Figure 9. Standard deviation of the size of the largest fragment, N_1, for the BPCA1 aggregate as a function of collision velocity v and scaled impact parameter b. The growth line, $n_{gr} = 1$, has been added for orientation as a dotted line.

collision channel only for large aggregates ($N \gtrsim 10^5$) and thus is of no concern for our collision simulations with $N = 20\,000$.

The average growth ratio of BPCA aggregates shows a slightly different velocity dependence than the homogeneous aggregates.

(i) At low velocities, $v \leq 5\,\mathrm{m\,s^{-1}}$, the growth ratio of BPCA aggregates is smaller than for homogeneous aggregates at all impact parameters, see Figs 2 and 8; actually $n_{gr} > 1$ for BPCA at these velocities. This is due to the fact that even large-impact parameter collisions have a high tendency for growth in BPCA aggregates due to the larger size and rough surface of these aggregates.

(ii) At large velocities, $v \geq 10\,\mathrm{m\,s^{-1}}$, BPCA aggregates feature a smaller growth ratio than the homogeneous aggregates, as could already be observed for central collisions, Fig. 2a.

Around the average growth velocity, $\langle v_{gr}\rangle = 7.5\,\mathrm{m\,s^{-1}}$, these two effects cancel. This argument helps explaining why the average growth velocity is similar for BPCA and homogeneous aggregates.

3.6 Ejecta

As grains are only loosely bonded to the aggregates, some of them will be emitted during the impact, as was already visible in the snapshots displayed in Figs 3 and 10. The majority of these ejecta consist of monomers, even though larger fragments are also ejected, as discussed above. The relative number of emitted monomers was termed 'shattering degree' by Osinsky & Brilliantov (2022). We display in Fig. 12 the average number of monomers ejected during the collision; this number has been averaged over the impact parameter, analogous to equation (7). A roughly linear increase with velocity is seen for all aggregate types.

Interestingly, the number of monomers is by more than 40 per cent larger for BPCA aggregates than for the homogeneous aggregates; this is a consequence of the more open structure of BPCA aggregates that allows dissociated grains to leave the collision zone while they are re-bonded to other grains in the homogeneous aggregates. The fractions of monomers ejected from the two classes of homogeneous aggregates, RPCA and LPCA, however are almost identical.

The spatial distribution of monomers ejected for central impacts is displayed in Fig. 13. At the velocity chosen, $5\,\mathrm{m\,s^{-1}}$, more than twice the number of monomers are ejected for BPCA aggregates than from RPCA aggregates. A clear difference between the ejection patterns
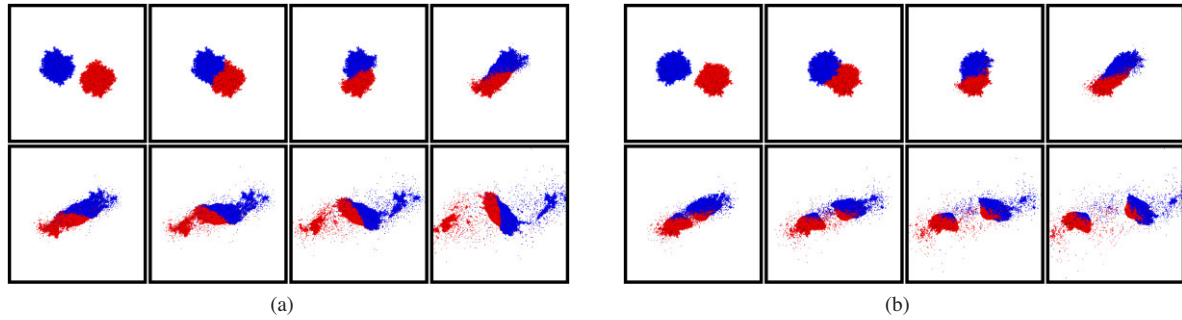
Figure 10. Series of snapshots (time difference 10 μs) showing the time evolution of BPCA aggregates at velocity $v = 5\,\mathrm{m\,s}^{-1}$ for an impact parameter of $b = 0.3875$. (a) shows the event with largest ($N_1 = 34057$) and (b) with the smallest ($N_1 = 23277$) fragment, while the average over all simulations is $\langle N_1 \rangle = 30606$. Grains are coloured according to their initial aggregate affiliation.
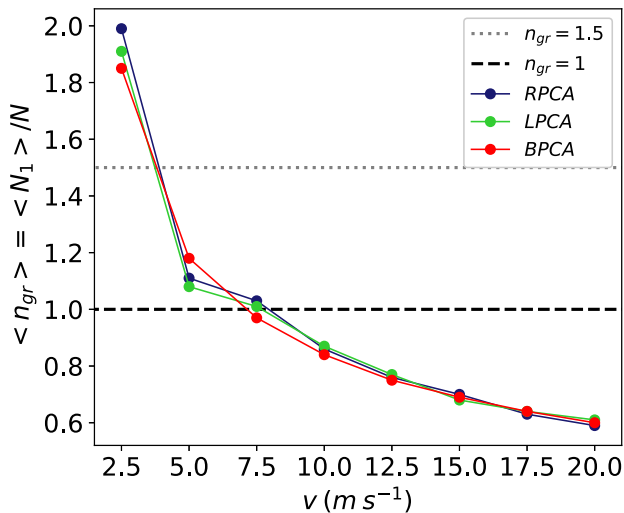

Figure 11. Impact-parameter-averaged growth ratio, $\langle n_{\mathrm{gr}} \rangle$, as a function of collision velocity v.
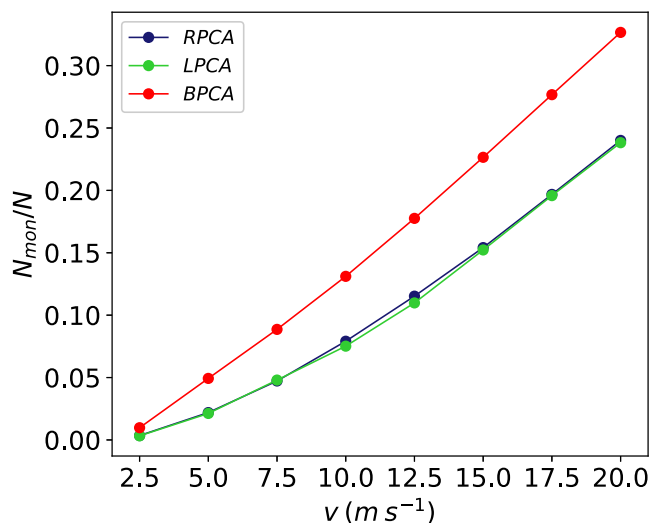

Figure 12. Impact-parameter-averaged fraction of ejected monomers as a function of the collision velocity v.

of RPCA aggregates, Fig. 13a, and BPCA aggregates, Fig. 13b, is observed. The emission from the homogeneous RPCA aggregates occurs mainly in a disc perpendicular to the velocity vector; this behaviour is typical of the emission patterns for central impact for such aggregates and is caused by ejection from the rim of the collision plane – this is the common tangent plane of the two aggregates at the point of contact – and in a direction parallel to the plane (Bandyopadhyay et al. 2023). In contrast, the BPCA-aggregate collision shows an additional quasi-isotropic emission distribution, which is caused by a more homogeneous ejection throughout the more porous aggregate surface.

In order to shed further light on the ejection process, Fig. 14 shows the dependence of monomer emission on both the collision velocity v and the scaled impact parameter b. Data are provided for a homogeneous aggregate (RPCA), Fig. 14a – the data for LPCA aggregates look quite similar and are not shown – and for BPCA aggregates, Fig. 14b. The maximum ejection occurs for slightly oblique impacts with an impact parameter around $b = 0.25$. This appears plausible, since at such intermediate impact parameters the collision zone – that is the overlap region of the two aggregates from which ejection may occur – is maximum; its size will decrease both for more central impacts, cf. Fig. 4, and for more glancing impacts. The similarity of the ejection data in Fig. 14 shows that the ejection mechanisms for BPCA and homogeneous aggregates are similar.

One might have expected that the distribution of coordination numbers in the aggregates is responsible for the differences in monomer ejection, as grains that have only one neighbour ($Z = 1$) would be more easily ejected than higher-coordinated grains. This is, however, not the case; as Fig. 1 showed, LPCA aggregates feature the highest fraction of singly connected grains, but their ejection patterns follow closely that of the RPCA aggregates with an order-of-magnitude less singly coordinated grains.

4 SUMMARY

We used granular-mechanics simulations to study the influence of the internal structure of an aggregate – in particular the grain coordination – on aggregate collisions when the total aggregate mass and the filling factor (at least in the central region) were kept fixed. We obtained the following findings.

(i) Central collisions of BPCA aggregates lead to slightly smaller fragments than for homogeneous aggregates. This feature also reduces the growth velocity of BPCA aggregates by around 10 per cent.
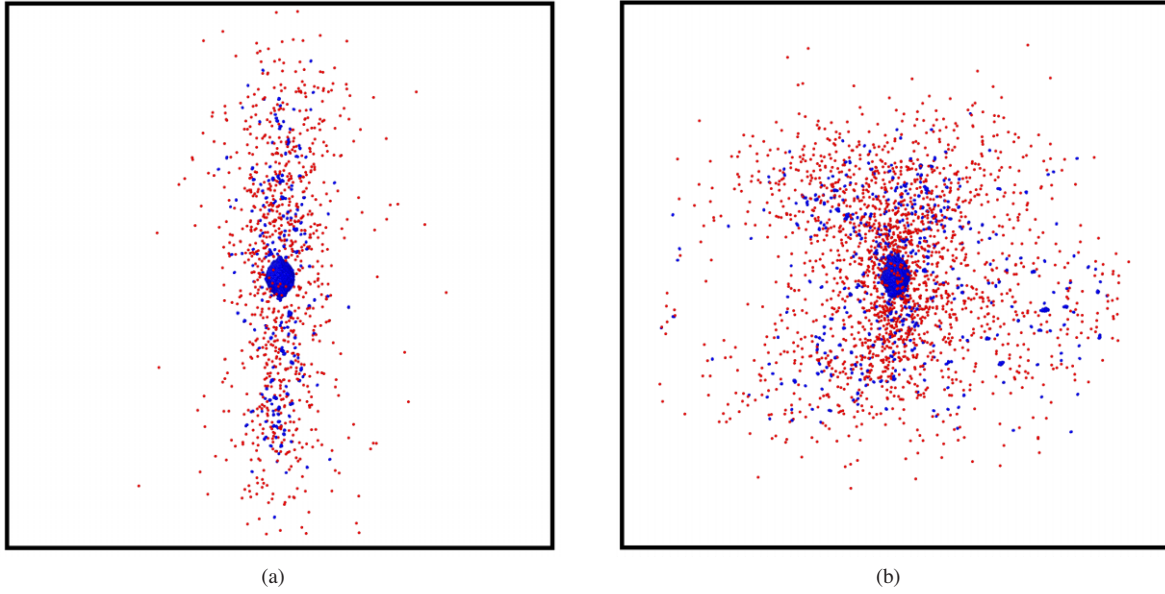
Figure 13. Final state after the collision of two (a) RPCA and (b) BPCA aggregates colliding centrally ($b = 0$) with a velocity of $5\,\mathrm{m\,s^{-1}}$. The initial velocity was in horizontal direction. Monomers are coloured red, grains in larger fragments blue.
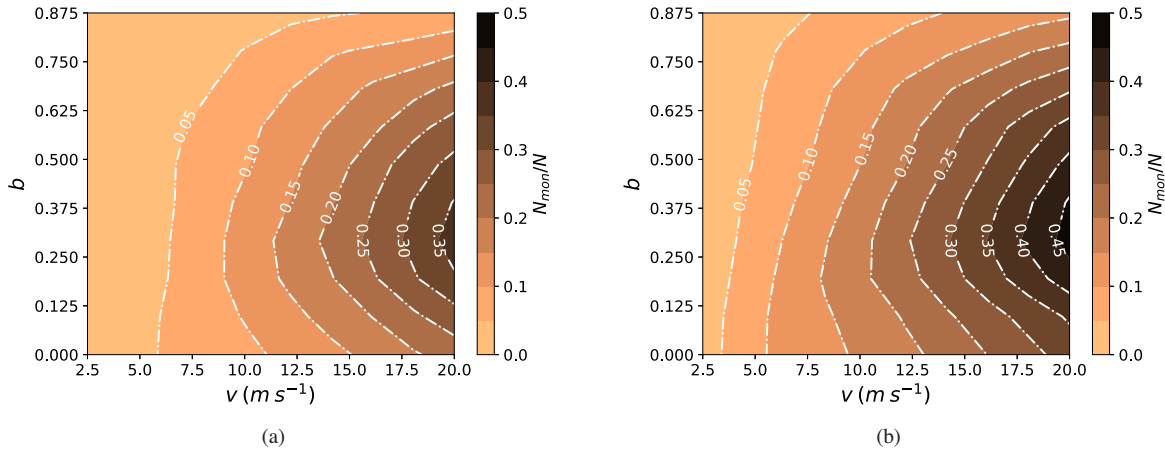

Figure 14. Dependence of the fraction of ejected monomers on collision velocity v and scaled impact parameter b for (a) RPCA and (b) BPCA aggregates.

(ii) If the collision velocity is scaled to the growth velocity at central impact, also for oblique collisions, the outcomes of BPCA aggregates vary only little from homogeneous aggregates.

(iii) Compaction in the collision zone is identical for all aggregates. The collision first dissociates the grains; these then aggregate again in a highly coordinated structure with a filling factor of around 0.52 and an average coordination $\langle Z \rangle \sim 4$.

(iv) For central collisions, fluctuations between individual collision events are similarly large for both types of aggregates. This demonstrates that variations between individual collision events are caused not so much by the internal aggregate structure but by the statistical nature of the aggregate fragmentation process.

(v) Fluctuations between individual collision events are largest along the 'growth line' $n_{\mathrm{gr}} = 1$ separating fusion events from sliding or fragmentation outcomes. Along this line, small deviations of grain positions may lead to different fragmentation processes even if the collision velocity and impact parameter are chosen identically.

(vi) Even for glancing collisions at low velocities, the larger extension and rough surface of BPCA aggregates does not cause major changes in the collision outcomes as compared to homogeneous aggregates with a well-defined and smooth surface.

(vii) The average growth velocity is independent of the aggregate type. Here two effects cancel: At high velocities, BPCA aggregates tend to erode more than homogeneous aggregates, while at small velocities even large-impact-parameter collisions lead to growth due to the large size and rough surface of BPCA aggregates.

(viii) Monomer ejection during the collision increases approximately proportional to collision velocity. It is enhanced by more than 40 per cent for BCPA aggregates relative to the homogeneous aggregates.

Comparison of our results to experiments is not readily performed since the internal aggregate structure is not so easily controlled in experiments. In addition, experiments are usually undertaken with massive aggregates containing a larger number of grains than

what is possible in simulation studies. Controlled laboratory experiments usually use aggregates with sizes larger than around 0.1 mm (Langkowski et al. 2008; Blum 2010; Beitz et al. 2011; Weidling et al. 2012; Schräpler, Landeck & Blum 2022), even though recently experiments on smaller aggregates were performed (Wurm & Teiser 2021), while simulations – such as ours – are restricted to smaller sizes, here of a few tens of μm. In this sense, our results are relevant for simulation studies as we showed that the internal aggregate structure is of little importance to the collision outcome, if appropriately scaled. Future experiments might explore small aggregates similar to the ones in this study, representing the early stages of aggregate evolution. Experiments might consider different aggregation scenarios which could lead to diverse agglomeration outcomes, corresponding to distinct astrophysical conditions.

Future simulations might explore collisional outcomes for much larger aggregates, with $N > 10^5$, where bouncing might occur (Arakawa et al. 2023) and could be influenced by aggregate topology.

Here we considered the impact between aggregates of the same size. However, our results for monomer ejection suggest that granular aggregate erosion by impacts with much smaller aggregates, or due to gas or plasma flows, might exhibit a stronger dependence on aggregate internal structure.

ACKNOWLEDGEMENTS

DATA AVAILABILITY

This study uses no data other than those generated in the simulation runs.

REFERENCES

Arakawa S., Okuzumi S., Tatsuuma M., Tanaka H., Kokubo E., Nishiura D., Furuichi M., Nakamoto T., 2023, ApJ, 951, L16
Armitage P. J., 2010, Astrophysics of Planet Formation. Cambridge Univ. Press, New York
Armitage P. J., 2011, ARA&A, 49, 195
Bandyopadhyay R., Urbassek H. M., 2023, MNRAS, 523, 365
Bandyopadhyay R., Umstätter P., Urbassek H. M., 2023, A&A, 672, A192
Beitz E., Güttler C., Blum J., Meisner T., Teiser J., Wurm G., 2011, ApJ, 736, 34
Bentley M. S., 2019, Aggregate. Available at: https://github.com/msbentley/aggregate
Berendsen H. J. C., 2011, A Student's Guide to Data and Error Analysis. Cambridge Univ. Press, Cambridge, p. 157
Birnstiel T., Fang M., Johansen A., 2016, Space Sci. Rev., 205, 41
Blum J., 2010, Res. Astron. Astrophys., 10, 1199
Blum J., 2018, Space Sci. Rev., 214, 52
Blum J., Schräpler R., 2004, Phys. Rev. Lett., 93, 115503
Burns J. A., Hamilton D. P., Showalter M. R., 2001, in Grün E., Gustafson B. Å. S., Dermott S., Fechtig H., eds, Interplanetary Dust. Springer, Berlin, p. 641
Chokshi A., Tielens A. G. G. M., Hollenbach D., 1993, ApJ, 407, 806
Dominik C., Tielens A. G. G. M., 1995, Phil. Mag. A, 72, 783
Dominik C., Tielens A. G. G. M., 1996, Phil. Mag. A, 73, 1279
Dominik C., Tielens A. G. G. M., 1997, ApJ, 480, 647
Gáspár A., Rieke G. H., Balog Z., 2013, ApJ, 768, 25
Grün E., 2007, in McFadden L. A., Weissman P. R., Johnson T. V., eds, Encyclopedia of the Solar System. Academic Press, New York, p. 621
Gunkelmann N., Ringl C., Urbassek H. M., 2016, A&A, 589, A30
Hasegawa Y. et al., 2023, ApJ, 944, 38
Hasegawa Y., Suzuki T. K., Tanaka H., Kobayashi H., Wada K., 2021, ApJ, 915, 22
Jutzi M., Holsapple K., Wünneman K., Michel P., 2015, in Michel P., DeMeo F. E., Bottke W. F. Jr, eds, Asteroids IV. Univ. Arizona Press, Tuscon, p. 679
Kloss C., Goniva C., Hager A., Amberger S., Pirker S., 2012, Prog. Comput. Fluid Dyn., 12, 140
Kozasa T., Blum J., Mukai T., 1992, A&A, 263, 423
Langkowski D., Teiser J., Blum J., 2008, ApJ, 675, 764
Meakin P., 1985, J. Colloid Interface Sci., 105, 240
Meakin P., 1999, J. Sol-Gel Sci. Technol., 15, 97
Millán E. N., Planes M. B., Urbassek H. M., Bringa E. M., 2023, A&A, 672, A50
Mukai T., Ishimoto H., Kozasa T., Blum J., Greenberg J. M., 1992, A&A, 262, 315
Ormel C. W., Paszun D., Dominik C., Tielens A. G. G. M., 2009, A&A, 502, 845
Osinsky A., Brilliantov N., 2022, Physica A: Stat. Mech. Appl., 603, 127785
Paszun D., Dominik C., 2009, A&A, 507, 1023
Planes M. B., Millán E. N., Urbassek H. M., Bringa E. M., 2020, MNRAS, 492, 1937
Planes M. B., Millán E. N., Urbassek H. M., Bringa E. M., 2021, MNRAS, 503, 1717
Ringl C., Urbassek H. M., 2012, Comput. Phys. Commun., 183, 986
Ringl C., Urbassek H. M., 2013, Comput. Phys. Commun., 184, 1683
Ringl C., Bringa E. M., Bertoldi D. S., Urbassek H. M., 2012, ApJ, 752, 151
Schräpler R. R., Landeck W. A., Blum J., 2022, MNRAS, 509, 5641
Tatsuuma M., Kataoka A., Tanaka H., 2019, ApJ, 874, 159
Tatsuuma M., Kataoka A., Okuzumi S., Tanaka H., 2023, ApJ, 953, 6
Wada K., Tanaka H., Suyama T., Kimura H., Yamamoto T., 2008, ApJ, 677, 1296
Wada K., Tanaka H., Suyama T., Kimura H., Yamamoto T., 2009, ApJ, 702, 1490
Wada K., Tanaka H., Suyama T., Kimura H., Yamamoto T., 2011, ApJ, 737, 36
Weidenschilling S. J., 1977, MNRAS, 180, 57
Weidenschilling S. J., Cuzzi J. N., 1993, in Levy E. H., Lunine J. I., eds, Protostars and Planets III. Univ. Arizona Press, Tuscon, p. 1031
Weidling R., Güttler C., Blum J., 2012, Icarus, 218, 688
Wurm G., Blum J., 1998, Icarus, 132, 125
Wurm G., Teiser J., 2021, Nat. Rev. Phys., 3, 405

This paper has been typeset from a TEX/LATEX file prepared by the author.